# Mammographic Image Denoising and Enhancement Using the Anscombe Transformation, Adaptive Wiener Filtering, and the Modulation Transfer Function

Larissa C. S. Romualdo · Marcelo A. C. Vieira · Homero Schiabel · Nelson D. A. Mascarenhas · Lucas R. Borges

Published online: 18 July 2012

© Society for Imaging Informatics in Medicine 2012

**Abstract** A new restoration methodology is proposed to enhance mammographic images through the improvement of contrast features and the simultaneous suppression of noise. Denoising is performed in the first step using the Anscombe transformation to convert the signal-dependent quantum noise into an approximately signal-independent Gaussian additive noise. In the Anscombe domain, noise is filtered through an adaptive Wiener filter, whose parameters are obtained by considering local image statistics. In the second step, a filter based on the modulation transfer function of the imaging system in the whole radiation field is applied for image enhancement. This methodology can be used as a preprocessing module for computer-aided detection (CAD) systems to improve the performance of breast cancer screening. A preliminary assessment of the restoration algorithm was performed using synthetic images with different levels of quantum noise. Afterward, we evaluated the effect of the preprocessing on the performance of a previously developed CAD system for clustered microcalcification detection in mammographic images. The results from the synthetic images showed an increase of up to 11.5 dB (p=0.002) in the peak signal-to-noise ratio. Moreover, the mean structural similarity index increased up to 8.3 % (p<0.001). Regarding CAD performance, the results suggested that the preprocessing increased the detectability of microcalcifications in mammographic images without increasing the false-positive rates. Receiver operating characteristic analysis revealed an

average increase of 14.1 % (p=0.01) in overall CAD performance when restored image sets were used.

 $\begin{tabular}{ll} \textbf{Keywords} & Image denoising} \cdot Quantum noise \cdot \\ & Computer-aided detection (CAD) \cdot Mammography \cdot \\ & Modulation transfer function \cdot Anscombe transformation \cdot \\ & Wiener filter \\ \end{tabular}$ 

## Introduction

Breast cancer is the most common cancer among women and one of the major causes of death among women worldwide [1]. When detected in its early stages, there is a 30 % chance that the cancer can be treated effectively, but the late detection of advanced-stage tumors makes treatment more difficult [2, 3]. X-ray mammography is the most used and the most effective technique for the early detection of breast cancer [4]. However, mammographic interpretation is a difficult task. Studies indicate that radiologists do not detect all abnormalities in mammographic images that are visible upon a retrospective review; the visual inspection of suspicious lesions can be very subtle, and the lesions are often masked by breast parenchyma [5]. False-negative rates for mammography range from 16 to 31 % [6].

To assist radiologists in mammogram interpretation, computer-aided detection (CAD) systems have been developed over the past 20 years [5, 6]. CAD is a computer-based system created to aid in the detection of suspicious lesions in mammographic images, providing a "second opinion" for the radiologist. Indeed, medical diagnoses are made by the radiologist, but he or she can use the output from a computer analysis of mammographic images to aid in his final decision [5]. Several studies have shown that the performance of radiologists in mammogram interpretation can be significantly improved when assisted by CAD, which demonstrates the

L. C. S. Romualdo  $\cdot$  M. A. C. Vieira ( $\boxtimes$ )  $\cdot$  H. Schiabel  $\cdot$  L. R. Borges

Electrical Engineering Department, University of São Paulo, USP, Av. Trabalhador São-Carlense, 400,

São Carlos, SP, Brazil e-mail: mvieira@sc.usp.br

N. D. A. Mascarenhas Computer Department, Federal University of São Carlos, UFSCar, Via Washington Luís, Km 235, São Carlos, SP, Brazil



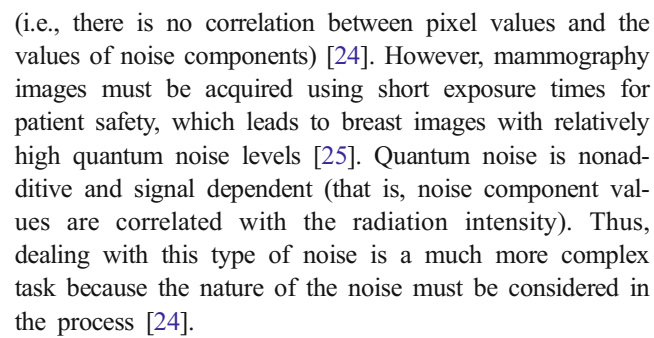
great potential of CAD to improve breast cancer screening [7, 8]. Currently, the sensitivity of CAD for breast cancer screening is relatively high (~90 %). However, specificity is too low, with approximately 400 false-positive marks to be dismissed for one cancer detected [9]. Thus, further efforts are needed to improve the specificity of CAD systems [5].

Among the lesions evaluated in mammographic reading, special attention is given to clustered microcalcifications because this arrangement is often associated with malignant tumors [10-12]. Due to their small size and mammographic image noise, the contrast between microcalcifications and breast tissue is relatively poor [11]. Microcalcifications may be inconspicuous and may be missed, even by a diligent radiologist [12]. The problem is worsened by dense-breast tissue. The presence of dense fibroglandular tissue in mammographic images can obscure signs of breast cancer and affect diagnostic accuracy [6, 13]. Although dense-breast tissue is normally found in women under 40 years old, hormonal reposition therapy has resulted in higher-thanexpected breast density in older women. Increases in breast density have been shown to reduce mammographic screening sensitivity and specificity [14, 15].

One of the main requirements to assure the better performance of CAD systems and thus improve medical diagnosis is to acquire good quality images [16]. Several researchers have reported that the characteristics of a mammographic image set can significantly affect the performance of a CAD system [17–19]. Digital mammograms with high spatial resolutions and low noise levels are required for accurate microcalcification detection by a CAD system [16]. For that reason, image processing algorithms for image enhancement and noise reduction have been utilized as preprocessing modules in CAD systems [20–23]. In this preprocessing step, the image contrast of breast lesions is enhanced, and CAD sensitivity in the detection of subtle cancers is improved.

However, for the proper use of preprocessing techniques in mammography images, some important aspects must be considered. First, image processing algorithms for the enhancement of high-frequency components, such as microcalcifications, have the undesirable effect of increasing image noise [24]. Thus, these algorithms may not only improve the CAD detection rate of suspicious lesions, particularly in dense-breast images but also typically increase the rate of false positives [21]. On the other hand, image processing algorithms for noise suppression typically reduce sharp transitions between pixel intensities, which results in image blurring [24]. This blurring impairs the detection of fine details and small structures in images. Thus, when utilizing CAD for microcalcification detection, noise reduction algorithms may reduce false-positive rates, but CAD sensitivity may be compromised.

Moreover, noise reduction techniques are generally based on the assumption that noise is additive and signal independent



Recently, a study showed that quantum noise is the dominant image quality factor in mammography and exerts a greater effect than spatial resolution when radiologists detect microcalcifications and discriminate between masses, impeding diagnostic performance [26]. Additionally, the reduction in false-positive rates is one of the main challenges of CAD systems, and the use of preprocessing techniques to improve the quality of images, making them more suitable for medical interpretation and computational analysis, is a tool that should be used.

In this context, this paper presents a restoration methodology to improve mammographic images based on a denoising algorithm followed by an enhancement technique. Noise reduction is performed in the first step using the Anscombe transformation [27, 28] to convert mammography quantum noise into Gaussian additive noise, which is filtered through an adaptive Wiener filter [28, 29]. In the second step, a filter based on the modulation transfer function (MTF) of the mammographic equipment in the whole radiation field is applied for image enhancement [30]. Thus, the proposed methodology can be used as a preprocessing module for CAD systems intended to improve breast cancer screening. In this paper, we focus on the enhancement of mammographic images and the influence of the proposed preprocessing algorithm on the improvement of CAD performance in clustered microcalcification detection.

## **Methods and Materials**

Image Denoising

The following model describes the image degradation process during acquisition [24]:

$$g(x,y) = f(x,y) * h(x,y) + n(x,y),$$
 (1)

where g(x,y) is the degraded image, f(x,y) is the input image, h(x,y) is the degradation function, n(x,y) is the additive noise and the operator "\*" indicates convolution. Restoration techniques usually manipulate this equation to obtain an estimate,  $\hat{f}(x,y)$ , of the input image when h(x,y) and n(x,y) are known [24].



The additive noise n(x,y) is incorporated by the digitization process and can be modeled as signal-independent Gaussian noise. However, f(x,y) cannot be considered a noise-free image because mammographic images are also corrupted by quantum noise, which is nonadditive noise and is normally modeled by a statistical Poisson distribution [25].

Furthermore, quantum noise is a signal-dependent noise because its variance is equal to the expected value, which is the rate of the signal. Therefore, the noise magnitude varies across the image, depending on the image intensity. The Anscombe transformation is a variance-stabilizing transformation that converts a random variable with a Poisson distribution into a variable with an approximately additive, signal-independent Gaussian distribution with 0 mean and unity variance [28].

Let the degraded image at coordinates x and y, g(x,y), be the random variable. Thus, the Anscombe transformation of g(x,y) is given by the following: [27]

$$z(x,y) = 2\sqrt{g(x,y) + \frac{3}{8}}. (2)$$

This equation can be represented by the following additive model [28]:

$$z(x,y) = \left(2\sqrt{r(x,y) + \frac{1}{8}}\right) + v(x,y)$$
  
=  $s(x,y) + v(x,y)$ , (3)

where r(x,y) is the rate of the Poisson-distributed image (i.e., the expected value) and v(x,y) is the additive term, which is independent of the signal s(x,y) and has an approximately Gaussian distribution [28]. After the Anscombe transformation, the additive term v(x,y) includes both the quantum noise converted into Gaussian noise and the electronic white noise, originally incorporated by the digitization process. Thus, this transformation allows for the use of any well-known denoising technique to reduce Gaussian additive noise by acting on the image z(x,y) in the Anscombe domain.

In this work, we used an adaptive Wiener filter to obtain an estimate,  $\widehat{s}(x,y)$ , of the expected noise-free mammographic image in the Anscombe domain. The Wiener filter calculates an estimate of a noise-free image that minimizes the mean squared error. Specifically, when z(x,y) is assumed to have a Gaussian additive noise, the Wiener filter is the optimal filter and is expressed as follows [29]:

$$\widehat{s}(x,y) = \overline{s}(x,y) + \frac{\sigma_s^2(x,y)}{\sigma_s^2(x,y) + \sigma_v^2(x,y)} [z(x,y) - \overline{z}(x,y)],$$
(4)

where  $\overline{s}(x,y)$  and  $\sigma_s^2(x,y)$  are the mean and variance of the signal, respectively;  $\overline{z}(x,y)$  is the mean of the image z(x,y); and  $\sigma_v^2(x,y)$  is the variance of the noise.

In the Anscombe domain, we can assume that  $\sigma_{\nu}^2(x,y)$  is equal to 1. Moreover,  $\overline{z}(x,y)$  is equal to  $\overline{s}(x,y)$  because the mean of the noise,  $\overline{v}(x,y)$ , is equal to 0. Thus, we can rewrite Eq. 4 as follows:

$$\widehat{s}(x,y) = \overline{s}(x,y) + \frac{\sigma_s^2(x,y)}{\sigma_s^2(x,y) + 1} [z(x,y) - \overline{s}(x,y)]$$
 (5)

Parameters  $\overline{s}(x, y)$  and  $\sigma_s^2(x, y)$  can be estimated by local statistics considering a small neighborhood around the pixel being processed. These required statistics should be calculated from the degraded image z(x,y) when the original signal is not known. In this case, these parameters could be calculated over a preliminary estimate of the signal,  $\hat{s}(x, y)$ , which can be obtained by blurring the image z(x,y) with a low-pass filter. In this work, we used a 3×3 averaging filter mask [24] on z(x,y) to obtain  $\hat{s}(x,y)$ , This filter was chosen because it is a simple smoothing filter and the size of the mask establishes the amount of blurring. The bigger the size of the average mask, the more noise will be removed to generate  $\widehat{s}(x,y)$ , but the restored image, at the end of the denoising procedure, will be more blurred. Thus, the 3×3 mask size generated a good estimation of s(x, y) without showing significant blurring.

Denoting the neighborhood around  $\widehat{s}(x,y)$  by  $A_{ij}$ , the local mean and variance of  $\widehat{s}(x,y)$  were estimated by:

$$\overline{s}(x,y) = \frac{1}{M^2} \sum_{i=0}^{M-1} \sum_{j=0}^{M-1} \widehat{\hat{s}}(i,j), \qquad i,j \in A_{ij}$$
 (6)

$$\sigma_s^2(x,y) = \frac{1}{M^2} \sum_{i=0}^{M-1} \sum_{j=0}^{M-1} \left[ \widehat{\overline{s}}(i,j) - \overline{s}(x,y) \right]^2, \qquad i,j \in A_{ij}$$
(7)

where M denotes the size of the square neighborhood  $A_{ij}$ .

The choice of the size M for local mean and variance estimation is crucial and has a great impact on the performance of the filter. The bigger the area of the neighborhood, the more noise will be removed, but the restored image will be more blurred. Thus, to properly define the size of the neighborhood  $A_{ij}$ , we considered the method originally proposed by Rabbani [31], where M is automatically adjusted depending on the signal activity in the neighborhood  $A_{ij}$ . Initially, the area  $A_{ij}$  is chosen to be a  $5\times 5$  square neighborhood around the pixel being processed (M=5). In that region, we measured the parameter  $\alpha(x,y)$ , which is defined as:

$$\alpha(x,y) = \frac{\widehat{\widehat{\sigma}}_r^2(x,y)}{\sigma_g^2(x,y)} \tag{8}$$

where  $\widehat{\sigma}_r^2(x,y)$  is the variance of the preliminary estimate of the rate of the signal in the spatial domain and  $\sigma_g^2(x,y)$  is the



variance of the degraded image in the spatial domain, both measured in the neighborhood  $A_{ij}$ . The preliminary estimate of the rate of the signal,  $\hat{r}(x,y)$ , was obtained by blurring the image g(x,y) with a  $3\times3$  averaging filter mask in the spatial domain.

The parameter  $\alpha(x, y)$  is in the range [0,1] and is a relative measure of the signal activity (variance) versus the noise variance [31]. Values of  $\alpha(x,y)$  close to 0 correspond to flat areas, with little signal variation compared to the variance of the noise. Conversely, the values of  $\alpha(x,y)$  close to 1 imply that the signal variance dominates the noise variance and are indicative of areas with fine details or sharp transitions. Thus, the size M of the square neighborhood around the pixel being processed in the Anscombe domain was chosen depending on the value of  $\alpha(x,y)$  (previously calculated in the spatial domain) following the algorithm proposed by Rabbani [31]. In this algorithm, if  $0.2 < \alpha(x,y) < 0.6$  (the values 0.2 and 0.6 were experimentally determined by the author), moderate signal activity is present and the required statistics were estimated from this 5×5 neighborhood using Eqs. 6 and 7. If  $\alpha(x,y) < 0.2$ , a relatively flat area was detected and the size of the square neighborhood was increased to 7×7 to enclose more pixels and to more effectively average out the noise. Finally, if  $\alpha(x,y) > 0.6$ , a possible sharp transition area has been encountered, and a set of gradient operations are performed on the pixels in the  $5 \times 5$  neighborhood to detect the gradient orientation. Then, this area is divided into two subregions and we considered only the subregion on the side of the sharp transition with average value more similar to the pixel being processed. The local mean and variance computed using this algorithm allowed the Wiener filter to reduce image noise without significantly affecting image sharpness.

After the adaptive Wiener filtering procedure, the inverse Anscombe transformation is applied to obtain the estimate,  $\hat{r}(x,y)$ , of an approximately noise-free mammographic image in the spatial domain. The inverse Anscombe transformation is described by the following equation: [27]

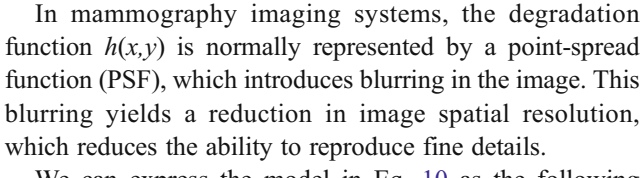
$$\widehat{r}(x,y) = \frac{1}{4}\widehat{s}(x,y)^2 - \frac{1}{8}$$
(9)

## MTF-Based Filtering

After noise removal by Wiener filtering in the Anscombe domain and assuming that the denoising procedure has not altered the degradation function, h(x,y), the model of image degradation described by Eq. 1 can be rewritten in the following form:

$$\widehat{r}(x,y) = f'(x,y) *h(x,y), \tag{10}$$

where  $\hat{r}(x,y)$  is the degraded mammographic image after denoising and f'(x,y) is the noise-free input image.



We can express the model in Eq. 10 as the following equivalent frequency domain equation:

$$\widehat{R}(u,v) = F'(u,v) \cdot H(u,v), \tag{11}$$

where the terms in capital letters are the Fourier transforms of the corresponding terms in Eq. 10 and u and v are the frequency variables. One benefit of using the Fourier transform for image restoration is that convolution in the spatial domain is analogous to multiplication in the frequency domain [24].

The Fourier transform of the PSF is the optical transfer function of the imaging system, whose magnitude is known as the MTF [30]. If the MTF of the imaging system is known and the degraded image has approximately no noise, the estimate  $\hat{F}'(u.v)$  of the original image in the frequency domain can be calculated by the simple restoration approach described by Eq. 12, which is known as the inverse filter [24]:

$$\widehat{F}'(u,v) = \frac{1}{\text{MTF}(u,v)} \cdot \widehat{R}(u,v)$$
(12)

Notice that a lot of the elements in MTF(u,v) could have values either at 0 or very close to it. Inverting these elements would give us either infinities or some extremely high values. Moreover, the inverse filtering could make the residual noise to dominate the estimate  $\widehat{F}'(u,v)$  near the high frequencies [24]. Thus, in order to avoid it, we considered a threshold by limiting the MTF(u,v) to values greater or equal to 0.5. In this case, we made MTF(u,v)=0.5 for all cases where MTF(u,v)<0.5.

To calculate the MTF(u,v) of mammography imaging systems, we considered two basic sources of image degradation in this study: (1) geometric unsharpness—the blurring caused by the finite size and the X-ray intensity distribution of the focal spot of mammographic equipment and (2) digitization unsharpness—the blurring due to the finite size of digital imaging detectors. Each individual source of degradation can be described by its own MTF. The MTF of the complete image system can be computed by multiplying the MTFs of the individual components of the system, as shown in the following equation [30]:

$$MTF(u, v) = MTF(u, v)_{Geometric} \cdot MTF(u, v)_{Digitization}$$
 (13)

Geometrical characteristics related to the radiographic exposure procedure cause the effective focal spot size (and hence the MTFs due to the geometric unsharpness) to vary



with the field location [32]. One solution for image restoration by the inverse filter is the division of the digital mammographic image into small regions ("sub-images"), in which the spatial invariance can be accomplished [33]. In this work, we considered square sub-images measuring 512×512 pixels as invariant regions (approximately 2.5×2.5 cm for an imaging system composed of 50-µm pixels). This size was chosen based on the performance of the Fast Fourier Transform algorithm. Sub-images were selected from the upper left region, and images were scanned from left to right and column by column down to the bottom, with the image oriented such that the breast was located on the left side of the image. Thus, we calculated the MTF for each region, and the restoration filter was applied individually for each sub-image, utilizing its own MTF.

# 1. Determining the MTF of the Geometric Unsharpness

The MTF of the geometric unsharpness was determined from the PSF resulting from the effective focal spot size and intensity distribution of the mammographic equipment. The procedures followed to measure the effective focal spot sizes have been specified by the National Electrical Manufacturers Association (NEMA) [34]. The recommended procedure requires that measurements be taken at the central beam position by using the slit camera technique. Those measurements should be made by utilizing at least two orientations of the slit: one parallel and the other perpendicular with respect to the cathode—anode axis [34].

Doi [32] showed that the PSF of geometric unsharpness at any arbitrary field position can be derived from that at the central beam position. Thus, we determined the PSF of geometric unsharpness according to the effective focal spot size calculated for the position corresponding to the center of each selected sub-image. We considered the effective focal spot at the central beam position to be a rectangle of dimensions a and b (Fig. 1) with a Gaussian distribution [35].

The next step was to calculate the effective focal spot sizes at the center of each sub-image. They can be derived from the dimensions measured at the central beam position, as shown in Fig. 1, using the following equations [32]:

$$a' = a \cdot \frac{1 + \cot \theta \cdot \frac{dx}{\text{SID}}}{\cos \gamma},\tag{14}$$

$$b' = b, (15)$$

where a and b are the effective focal spot sizes at the central beam position, measured at the parallel and perpendicular orientations, respectively, with respect to the cathode–anode axis; a' and b' are the new dimensions of the effective focal spot calculated for an arbitrary field position (dx,dy), which corresponds to the center of the selected sub-image; SID is

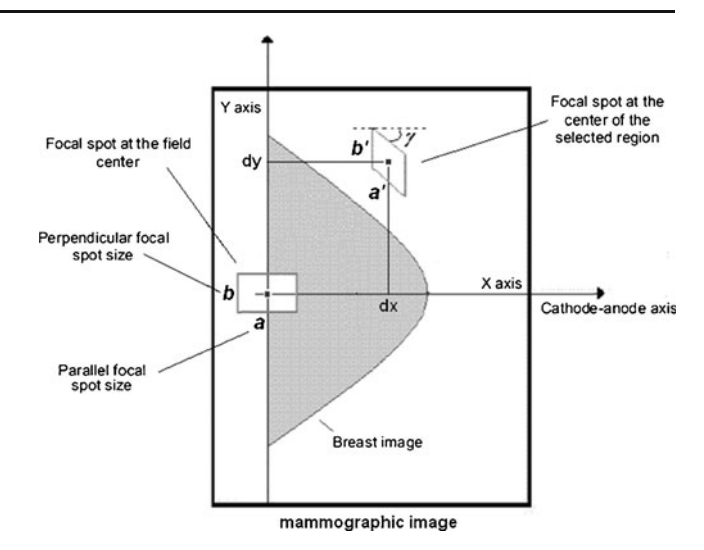


Fig. 1 The effective focal spot sizes (a',b') and the skew angle  $\gamma$  at the arbitrary position (dx,dy) can be derived from those measured at the center of the field

the source-to-image distance; and  $\theta$  is the anode angle. Furthermore, depending on the field position, the shape of the effective focal spot can be skewed by the angle  $\gamma$ , as shown in Fig. 1, which can be calculated using the following equation [32]:

$$\gamma = \tan^{-1} \left( \frac{dy}{dx + \text{SID} \cdot \tan \theta} \right). \tag{16}$$

After determining the effective focal spot sizes at each position, the next step is to calculate the magnitude of the corresponding geometric unsharpness ( $U_{a'}$  and  $U_{b'}$ ) for both orientations. The calculation is performed by considering the relationship between the dimensions of the effective focal spot and the enlargement factor to which the internal breast structures are subjected during radiographic imaging. This factor is calculated by considering the relationship between the object-to-image distance (OID) and the source-to-object distance (SOD), as shown in Fig. 2, using the following equation [36]:

$$U_{a',b'} = (a',b') \cdot \frac{\text{OID}}{\text{SOD}} \tag{17}$$

The term "object" refers to any structure inside the breast. However, during radiographic imaging, there is a superposition of these structures because they are projected onto a flat, two-dimensional image. Thus, the geometric unsharpness for each structure depends on the height at which it is located inside the breast. Nevertheless, accurately determining this positioning for each structure is almost impossible from the analysis of a flat image. Thus, in this work, we considered the plane cutting the center of the compressed breast as an object to calculate the geometric unsharpness of structures, as shown in Fig. 2.



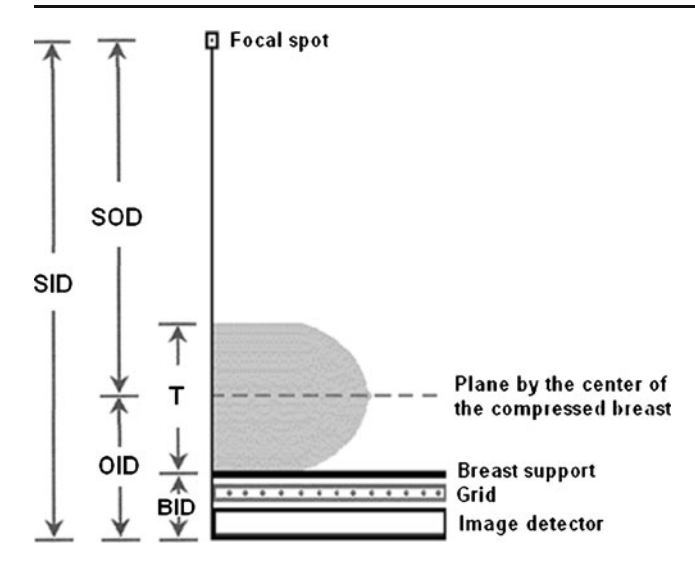


**Fig. 2** The enlargement factor considered for breast imaging. *T* corresponds to the compressed breast thickness, and BID corresponds to the distance between the breast support and the image detector. The geometric unsharpness depends on the effective focal spot size and the relationship between the object-to-image distance (OID=BID+*T*/2) and the source-to-object distance (SOD=SID-OID), as shown in Eq. 17

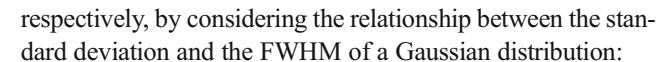
The OID is calculated by summing the distances from the breast support to the image detector (BID) with half of the compressed breast thickness (T/2). In this work, the enlargement factor was calculated by considering a 4.5-cm compressed breast. The values for SID and BID were measured in each mammography unit.

The final step is to calculate the  $PSF(x,y)_{Geometric}$  and thus the  $MTF(u,v)_{Geometric}$  due to the geometric unsharpness. By determining the magnitude of the geometric unsharpness from Eq. 17, the  $PSF(x,y)_{Geometric}$  for each sub-image was simulated considering the focal spot having a Gaussian intensity distribution [35]:

$$PSF(x,y)_{Geometric} = e^{-\left(\frac{x^2}{2(\sigma_x)^2} + \frac{y^2}{2(\sigma_y)^2}\right)},$$
(18)

where  $\sigma_x$  and  $\sigma_y$  are the standard deviations of the Gaussian intensity distribution along x and y, which correspond to the parallel and perpendicular orientation at the field, respectively, relative to the cathode–anode axis (see Fig. 1).

Although the NEMA standard does not provide criteria for determining the width of the slit image when measuring effective focal spot sizes, it has been a general practice to measure the dimension of a slit image by considering the full width at half maximum (FWHM) [37]. In this work, we determined the effective focal spot sizes of all mammographic equipment by measuring the FWHM of the slit image profile [38]. Thus, to correctly simulate the PSF(x,y)<sub>Geometric</sub> using Eq. 18, the standard deviations  $\sigma_x$  and  $\sigma_y$  were derived from the magnitude of the geometric unsharpness  $U_{a'}$  and  $U_{b'}$ ,



$$\sigma_{x,y} = \frac{U_{a',b'}}{2\sqrt{2\ln 2}} \tag{19}$$

Finally, the MTF(u,v)<sub>Geometric</sub> due to geometric unsharpness was calculated by applying the two-dimensional Fourier transform to the PSF(x,v)<sub>Geometric</sub>.

# 2. Determining the MTF of the Digitization Unsharpness

The MTF of the digitization unsharpness can be determined from the PSF through either the finite size of imaging detectors, if we consider the digital mammography systems, or the film digitizer spatial resolution, if we consider the digitized screen-film mammography images. We simulated the PSF(x,y)<sub>Digitization</sub> by considering a squared PSF with a uniform intensity distribution, whose sizes correspond to the pixel size actually used in the image digitization. Thus, due to the digitization unsharpness, MTF(u,v)<sub>Digitization</sub> was calculated using the Fourier transform. By determining the MTF of the geometric and the digitization unsharpness, the MTF of the complete image system was calculated using Eq. 13.

Finally, mammographic images were restored in the frequency domain using the proposed MTF-based filtering. The Fourier transform was applied to each sub-image extracted from the original image after denoising. Next, the inverse filter of Eq. 12 was applied using its own MTF. Each calculated MTF was properly analyzed to avoid zero or very small values before applying the inverse filter, as stated above. Finally, the inverse Fourier transform was used to obtain the resulting restored image,  $\hat{f}'(x,y)$ .

## Results

A preliminary assessment of the proposed restoration algorithm was performed using synthetic images. We generated degraded images with known levels of blurring and quantum noise and compared them to the reference images to evaluate how the preprocessing technique could improve image quality. Afterward, we evaluated the effect of the preprocessing on the performance of a previously developed CAD system for clustered microcalcification detection [39, 40].

## **Evaluation Using Synthetic Images**

To evaluate the performance of the proposed restoration algorithm, we generated synthetic images (512×512 pixels, 8 bits) blurred by a Gaussian low-pass filter and corrupted by different levels of quantum noise. All images were



restored using the proposed methodology. Figure 3 shows one example of these synthetic images: on the top left is the original ground truth image without any blur or noise used as a reference; on the top right is the same image plotted as a

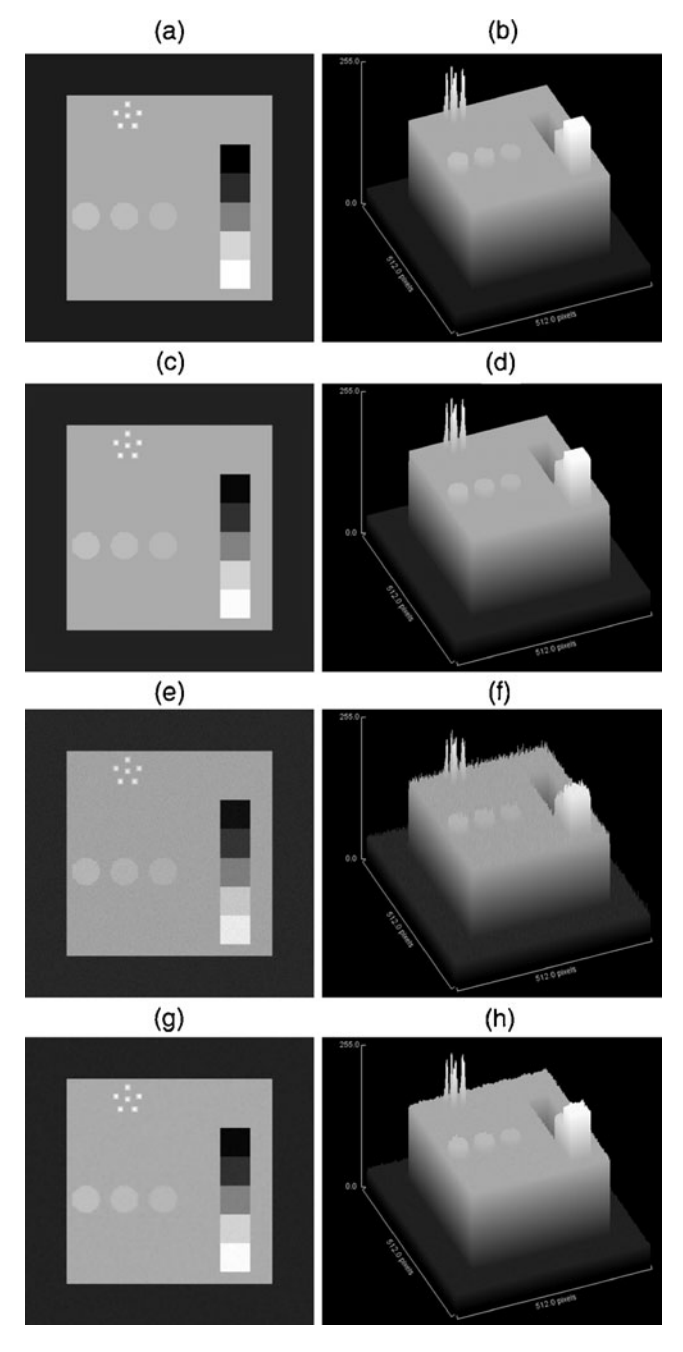


Fig. 3 Examples of synthetic images used for preliminary assessment of the proposed restoration algorithm. a Original image without any blur or noise: used as a reference; **b** reference image plotted as a surface; **c** blurred image: corrupted by a Gaussian low-pass filter; **d** blurred image plotted as a surface; **e** degraded image: blurred by a Gaussian low-pass filter and corrupted by quantum noise with a magnitude corresponding to approximately 25 % of the normal clinical dose for mammography; **f** degraded image plotted as a surface; **g** restored image; **h** restored image plotted as a surface

surface; in the second line is the blurred image, corrupted by the Gaussian PSF(x,y) of Eq. 18 with  $\sigma_x = \sigma_y = 4$  pixels and the corresponding surface plot; in the third line is the blurred image additionally corrupted by quantum noise generated by a radiation exposure of 5,665 photons/pixel on average, which corresponds to approximately 25 % of the normal clinical dose for mammography and the corresponding surface plot; and on the bottom is the resulting image after preprocessing the degraded image showed in the third line using the restoration technique proposed in this work and the corresponding surface plot. The results presented in Fig. 3 show that the proposed restoration algorithm notably reduced image noise and preserved the fine details and sharp transitions in the image, even for an image corrupted by a high level of quantum noise (representing 25 % of the normal radiation dose for mammography).

Objective methods used to evaluate image restoration techniques normally quantify the differences (error) between the restored image,  $\hat{f}(x,y)$ , and the reference image (ground truth), f(x,y), using a variety of signal fidelity measurements. The goal of a signal fidelity measurement is to compare two signals by providing a quantitative score that describes the degree of similarity between them [41]. To perform an objective assessment on the performance of the proposed restoration methodology, we calculated the following signal fidelity measures using synthetic images: peak signal-to-noise ratio (PSNR) [41] and mean structural similarity index (MSSIM) [42].

The PSNR is an important metric for characterizing the performance of image restoration algorithms. It represents the ratio between the maximum possible power of a signal and the power of corrupting noise that affects the fidelity of its representation. A higher PSNR would normally indicate a restoration of higher quality [41]. The SSIM index includes human visual perception in the measurement extracting information about the luminance, contrast, and structure of an image. It was designed to improve traditional signal fidelity measures. SSIM is calculated on various windows of both restored and reference images. Typically, it is calculated on window sizes of 8×8, which should be displaced pixel-by-pixel in both images. In practice, the mean value of the SSIM indexes (MSSIM) of all windows is used to evaluate the overall image quality. The resultant MSSIM index is a decimal value between -1 and 1, where a value of 1 can be reached only in the case of two identical images [42].

In this study, we considered four different synthetic images which were degraded by a Gaussian low-pass filter (PSF(x,y)) of Eq. 18 with  $\sigma_x = \sigma_y = 4$  pixels) and by three levels of simulated quantum noise, totalizing 12 synthetic images. We considered the quantum noise levels representative of approximately the normal clinical dose for mammography (22,660 photons/pixel in the average), 50 % of the normal dose (11,330 photons/pixel in the average), and



25 % of the normal dose (5,665 photons/pixel in the average). Ideal synthetic images without any blur or noise were also generated to provide the ground truth reference.

All synthetic images were restored by considering three image restoration techniques: (1) images processed by the proposed MTF-based filter but using an average filter mask  $3 \times 3$  for denoising; (2) images processed by the Wiener filter in the frequency domain, using an algorithm developed in a previous work [43]; and (3) images processed by the MTFbased filtering after image denoising by Anscombe transformation and adaptive Wiener filtering, as proposed in the present work. Table 1 shows the average values of PSNR and MSSIM measurements calculated for the synthetic images before and after restoration using these three preprocessing methodologies. The relative improvement in image quality provided by these image restoration techniques was also calculated. Paired two-tailed Student's t test was used to evaluate if the signal fidelity measurements using degraded and restored images were statistically significant.

As expected, Table 1 shows that the synthetic images acquired with higher levels of quantum noise (lower radiation dose) produced worst image quality index values calculated before restoration. This result indicates that mammography quantum noise is signal dependent and increases with a reduction in radiation dose. Table 1 shows that the relative improvement in image quality achieved using all of the restoration techniques was higher for images with lower simulated dose. However, we note that the improvement in image quality was notably better when our preprocessing methodology was used for image restoration. We observed an increase of up to 11.5 dB in the PSNR measurements after restoration (p=0.002). Moreover, the

MSSIM index increased up to 8.3 % (p<0.001). In this case, quantum noise was reduced without significantly affecting the image sharpness (Fig. 3).

The lowest signal fidelity values were obtained when the MTF-based filter was employed on images after denoising by an average 3×3 filter mask. This result indicates that the average mask filtering is not appropriated for Poisson noise removal and that it produces significant blurring in the image that cannot be properly recovered by the MTF-based filter. Denoising using this type of filter worsened image quality. When comparing the results using the Wiener filter in the frequency and Anscombe domains, we observed that the Wiener filter achieved much better noise reduction when applied in the Anscombe domain using the adaptive methodology proposed in this work.

## Evaluation Using a CAD System

After the preliminary assessment of the proposed image restoration methodology using synthetic images, we evaluated the effect of this restoration technique on the performance of a previously developed CAD system for microcalcification detection [39, 40]. The main objective was to compare the improvement in CAD performance when using the restored images instead of the degraded ones. Then, two mammographic image sets were considered in this study. The first one consisted of digital mammographic images of a tissue-equivalent breast phantom acquired through three different magnitudes of radiation dose, providing three different levels of quantum noise. The other image set consisted of real breast images extracted from an online mammographic image database [44]. All of the

Table 1 Results of PSNR and MSSIM measurements for the synthetic images and the relative improvement achieved after preprocessing using three different image restoration techniques, including the one proposed in this work

Restoration method	Radiation dose	Signal fidelity measurements							
		PSNR (dB)				MSSIM			
		Before restoration	After restoration	Relative improvement (dB)	p value	Before restoration	After restoration	Relative improvement (%)	p value
Average mask 3 x 3 and MTF-based filter	Normal	44.04	38.08	-5.96	0.03	0.9772	0.9807	+0.36	0.24
	50 %	42.02	37.95	-4.07	0.12	0.9571	0.9723	+1.59	0.04
	25 %	39.70	37.72	-1.98	0.42	0.9201	0.9426	+2.45	0.04
Wiener filter in frequency domain	Normal	44.04	45.03	+0.99	0.17	0.9772	0.9866	+0.96	0.004
	50 %	42.02	44.17	+2.15	0.004	0.9571	0.9789	+2.28	0.003
	25 %	39.70	42.39	+2.69	0.003	0.9201	0.9708	+5.51	< 0.001
Proposed method	Normal	44.04	54.37	+10.33	0.004	0.9772	0.9987	+2.20	< 0.001
	50 %	42.02	53.00	+10.98	0.003	0.9571	0.9980	+4.27	< 0.001
	25 %	39.80	51.27	+11.47	0.002	0.9201	0.9966	+8.31	< 0.001

Images were degraded by a low-pass Gaussian filter and quantum noise of three different levels



images from both databases were restored by the proposed methodology, and we compared CAD performance using degraded and restored images to evaluate how the preprocessing technique could improve the performance of a CAD system for mammography.

## 1. Phantom Image Set

Phantom images were acquired using a CIRS Tissue-Equivalent Phantom for Mammography, model 011A (Computerized Imaging Reference Systems, Inc. Norfolk, VA). This phantom represents a compressed breast measuring 4.5 cm in thickness with an adipose-to-glandular ratio of 50:50 [45]. This type of phantom was chosen because of its tissue equivalency and realistic breast shape and because it contains several components that closely mimic the radiographic properties and shapes of normal and pathological breast structures. This phantom image shows 12 clusters of specks, each consisting of six specks, simulating 72 microcalcifications with a grain size ranging from 0.130 to 0.400 mm [45].

Digital mammographic images of this phantom were acquired through a *Lorad M-III* mammographic unit (*Hologic*, Inc. Bedford, MA) using an Agfa computed radiography (CR) system consisting of a *CR MM3.0 Mammo plate* and a *CR 85-X Digitizer* (*Agfa-Gevaert Group*, Mortsel, Belgium). Images

Fig. 4 Region extracted from one mammographic image of a CIRS tissue-equivalent phantom showing the effect of the proposed restoration technique. a Degraded image acquired with approximately 25 % of the normal clinical dose for mammography; b degraded image plotted as a surface; c restored image; d restored image plotted as a surface

were acquired at 26 kVp using three different dose levels, which were provided by considering the normal dose automatically adjusted by the mammographic unit automatic exposure controller (AEC) (exposure using 180 mAs), 50 % of the normal dose (90 mAs), and 25 % of the normal dose (45 mAs). Digital images presented 4,096 gray levels (12 bits) and a pixel size of 50  $\mu m$ . Thus, the images allowed for the quantitative analysis of CAD performance in detecting microcalcifications using degraded and restored images considering different levels of quantum noise.

Some physical parameters of the mammographic unit and the acquisition system were measured using previously developed methodologies for quality assurance [46, 47]. These measurements were important because the proposed restoration method uses information about the image acquisition system to produce the MTF-based filter, as described before. The measured parameters include the effective focal spot sizes at the center of the field, anode angle ( $\theta$ ), SID, BID, and the exact location of the center of the field.

Figure 4 shows one example of a region (1,900×1,900 pixels) extracted from the mammographic image of the breast phantom acquired with quantum noise levels representative of approximately 25 % of the normal clinical dose for mammography (26 kVp–45 mAs). On the top left is the degraded image (originally taken with no preprocessing); on the top right is the same image plotted as a surface; on the bottom left is the

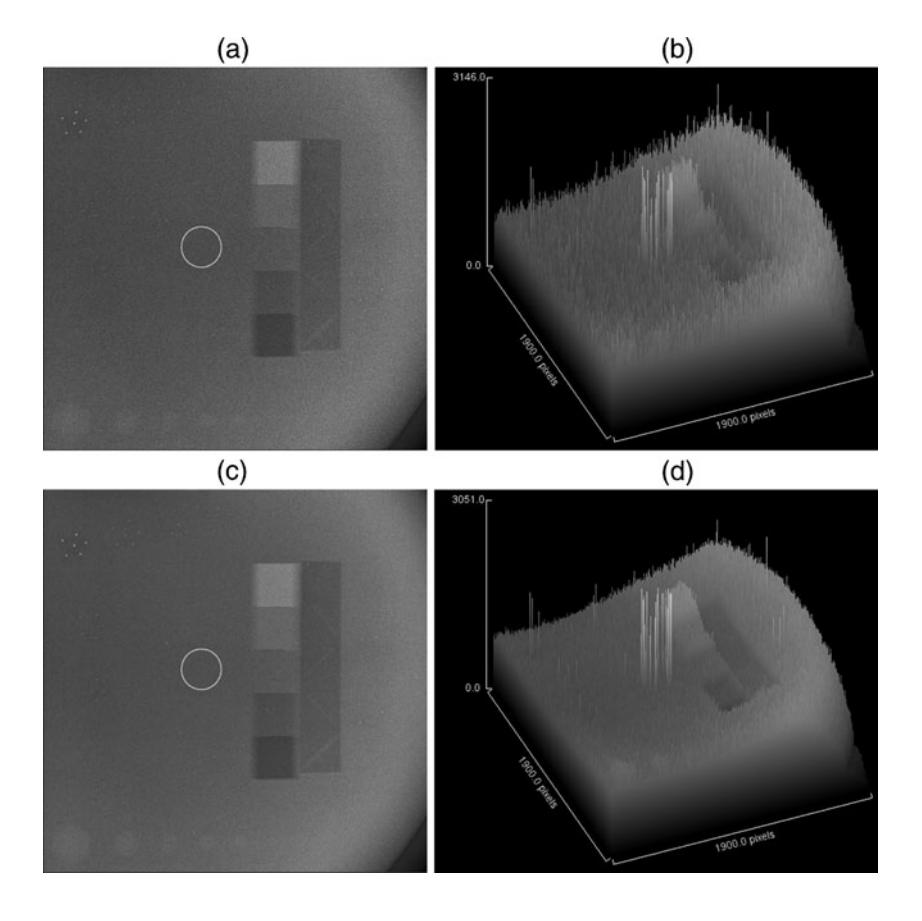




Table 2 CAD sensitivity and specificity for microcalcification detection in both degraded and restored breast phantom images acquired with three different levels of quantum noise

Radiation dose	True-positiv	re rates	False-positive rates		
	Degraded	Restored	Degraded	Restored	
Normal	0.806	0.931	0.042	0.014	
50 %	0.681	0.917	0.111	0.097	
25 %	0.375	0.792	0.055	0.055	

restored image after using the preprocessing technique proposed in this work; and on the bottom right is the restored image plotted as a surface. Figure 4 shows that the restoration algorithm proposed in this work led to microcalcifications appearing more visible in this mammographic image. Restoration reduced image noise without significantly affecting image sharpness, even for an image corrupted by a high level of quantum noise (representing 25 % of the normal radiation dose for mammography).

All acquired mammographic images of the breast phantom database were restored by the proposed methodology and analyzed by the CAD system for automatic microcalcification detection. We compared the number of microcalcifications correctly detected using the degraded and the restored images. Thus, from the results of the digital processing, the number of structures correctly detected in both cases could be quantified, and we could evaluate the impact of the preprocessing on CAD performance regarding microcalcification detection. We evaluated the CAD performance in terms of CAD sensitivity (truepositive rates) and specificity (false-positive rates) using the receiver operating characteristic (ROC) analysis (Table 2) [48]. ROC curves are frequently used to describe and compare the performance of diagnostic algorithms. In this study, the variable criterion for determining the ROC curves was the sensitivity of the segmentation algorithm inside the CAD system, which determines the number of signals kept in the image [21]. Figures 5, 6, and 7 show the calculated ROC curves of the CAD performance for the degraded and restored breast phantom images with different levels of quantum noise; the images were acquired using AEC normal radiation dose, 50 % of the normal dose, and 25 % of the normal dose, respectively. Additionally, the area under the ROC curves (Az) was measured. Az is a parameter commonly used to evaluate and compare the overall performance of CAD systems [5, 21, 23]. These ROC curves were generated using a web-based calculator provided by the Johns Hopkins University [49].

The results presented in Table 2 show that CAD performance for the detection of microcalcifications in the phantom images depended on image noise: images with higher quantum noise (less radiation dose) yielded a worse CAD detection rate. After restoration, CAD sensitivity was improved regardless of the quantum noise level of the degraded image. CAD

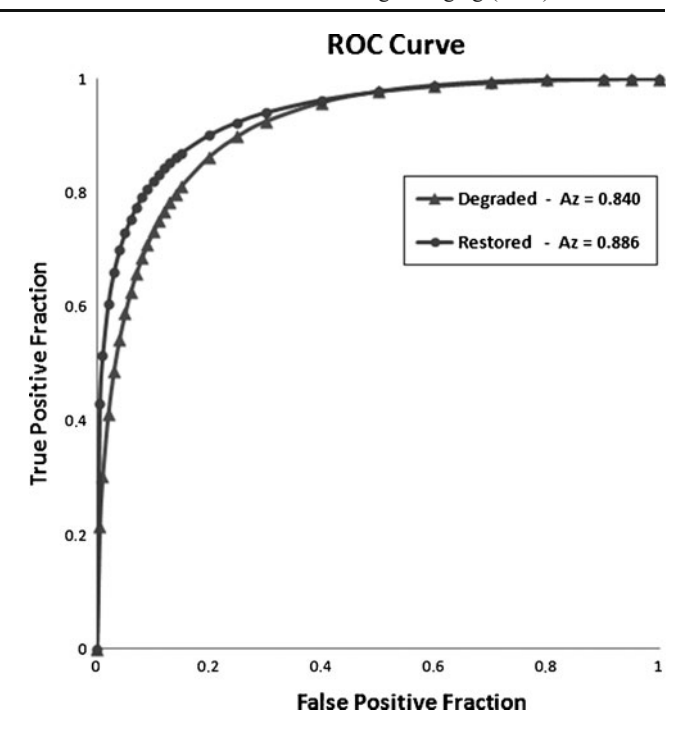
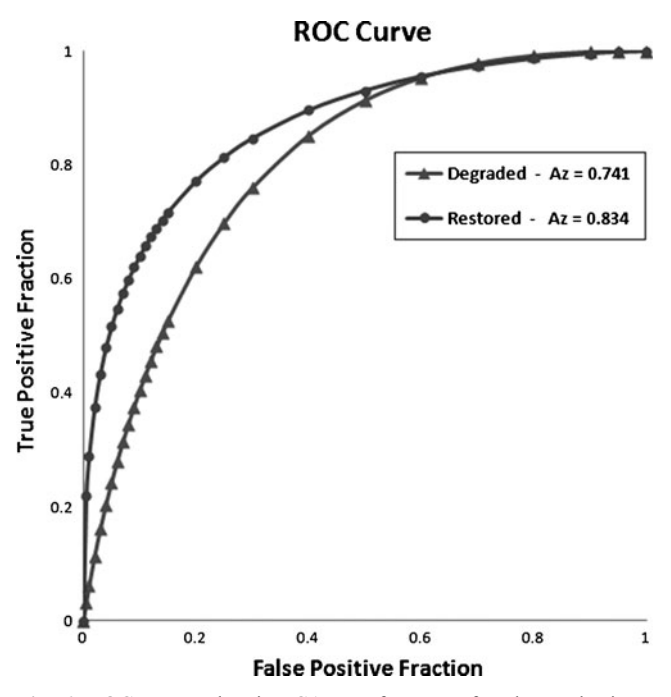


Fig. 5 ROC curves showing CAD performance for clustered micro-calcification detection in the phantom images acquired at normal radiation dose. Degraded images (filled triangles) (originally taken with no preprocessing) and restored images (filled circles). The parameter Az corresponds to the area under the ROC curve

specificity was also improved for phantom images acquired using the normal dose and 50 % of the normal dose.



**Fig. 6** ROC curves showing CAD performance for clustered microcalcification detection on the phantom images acquired at 50 % of the normal radiation dose. Degraded images (*filled triangles*) (originally taken with no preprocessing) and restored images (*filled circles*). The parameter Az corresponds to the area under the ROC curve



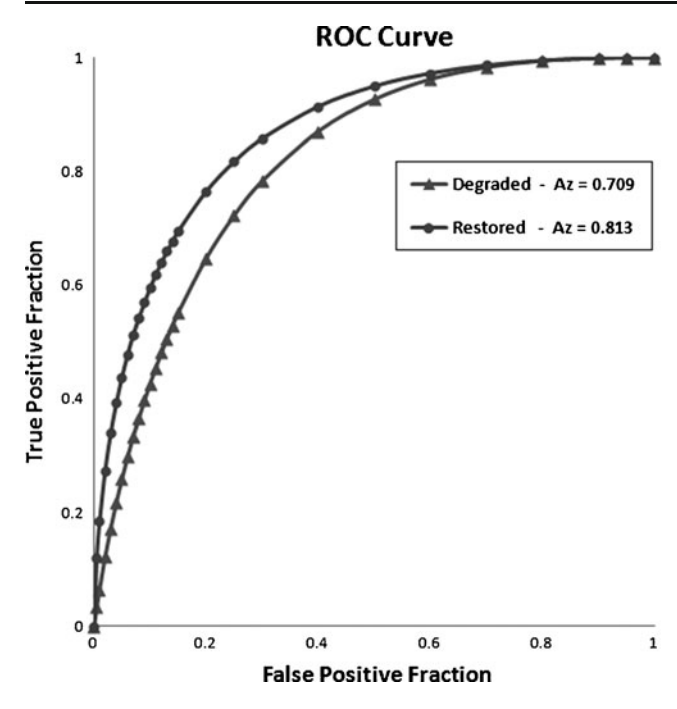


**Fig.** 7 ROC curves showing CAD performance for clustered microcalcification detection on the phantom images acquired at 25 % of the normal radiation dose. Degraded images (*filled triangles*) (originally taken with no preprocessing) and restored images (*filled circles*). The parameter Az corresponds to the area under the ROC curve

The ROC curves show that the preprocessing technique increased overall CAD performance for all three cases. We observed an average increase of 10.9 % (p=0.04) in CAD performance, measured using the area under the curve (Az), when the restored phantom images were used (Figs. 5, 6, and 7).

#### 2. Real Breast Image Set

After evaluating CAD performance using the breast phantom images, we investigated the improvement in CAD detection when the proposed restoration technique was performed on real breast images. Thus, we selected 128 breast images from an online mammographic images database previously developed to test and evaluate CAD systems [44]. For this study, we selected only dense-breast images used in real mammography examinations acquired at three different hospitals (and three different imaging systems), all of them with clustered microcalcifications. This type of image was chosen because microcalcification

Table 3 Physical characteristics of the mammographic units and film digitizers used to acquire the real breast image set

Hospital no.	Mammographic unit	Effective focal spot sizes (mm)	Number of images selected	Pixel size (mm)	Gray levels (12 bits)
1	Lorad M-III	$0.65 \times 0.32$	48	0.150	3,600
2	GE Senographe 600t	$0.52 \times 0.45$	48	0.150	3,600
3	Philips MD4000	$0.54 \times 0.30$	32	0.085	3,800

detection in dense-breast images remains a challenge for CAD systems. Studies have shown that CAD sensitivity and specificity decrease considerably when using dense-breast images because it is more difficult to detect small lesions in images with low contrast and high levels of noise [6, 15, 20]. Information regarding mammographic findings, breast density, and pathologies was obtained from this database and was extracted from physicians' reports and confirmed by previous and later exams, including follow-up mammography, ultrasound exam, and/or biopsy [44].

Again, some physical parameters of those mammographic units and film digitizers used in this study had to be measured because the proposed restoration method uses information about the image acquisition system to produce the MTF-based filter, as described above. Because each hospital had its own equipment to acquire digital mammograms, we developed a database that contained all the physical parameters of the image acquisition system, which is important to the restoration algorithm in automating the restoration procedure. Table 3 shows some characteristics of the real breast image set used in this study.

Mammographic images were grouped according to the hospital from which the mammograms were originally obtained. All of the images were restored by the proposed methodology and were processed by the CAD system to detect clustered microcalcifications. We compared the performance of the CAD system using the degraded and the restored images. Thus, from the results of CAD analysis, we calculated CAD sensitivity and specificity using ROC analysis (Table 4). Figures 8, 9, and 10 show the calculated ROC curves for the dense-breast image groups taken from hospital nos. 1, 2, and 3, respectively, considering the degraded and the restored images. The area under the ROC curves (Az) was also measured.

Table 4 shows that CAD performance was relatively poor when dense-breast images were used. However, preprocessing yielded an increase in CAD true-positive rates and a decrease in CAD false-positive rates for the three image groups considered in this study. Moreover, the ROC curves show that the parameter Az was higher when restored mammographic images were used. We observed an average increase of 14.1 % (p=0.01) in overall CAD performance (Figs. 8, 9, and 10) when the restored real breast image set was used.



**Table 4** CAD sensitivity and specificity for clustered microcalcification detection in both degraded and restored real breast images acquired using three different mammography imaging systems

Hospital no.	True-positive	rates	False-positive rates		
	Degraded	Restored	Degraded	Restored	
1	0.655	0.793	0.172	0.138	
2	0.690	0.862	0.310	0.241	
3	0.758	0.897	0.483	0.379	

## Discussion

The improvement in mammographic image quality resulting from the proposed restoration method was evaluated. Preliminary tests were performed by comparing the original and the restored synthetic images in terms of several widely used signal fidelity measurements. Afterward, we compared the performance of a previously developed CAD system for microcalcification detection when using degraded and restored mammographic images from two different databases: a breast phantom image set and a real breast image set.

The results regarding synthetic images corrupted by different levels of quantum noise showed that our preprocessing methodology produced restored images significantly more similar to the reference images than the other restoration techniques considered in this study.

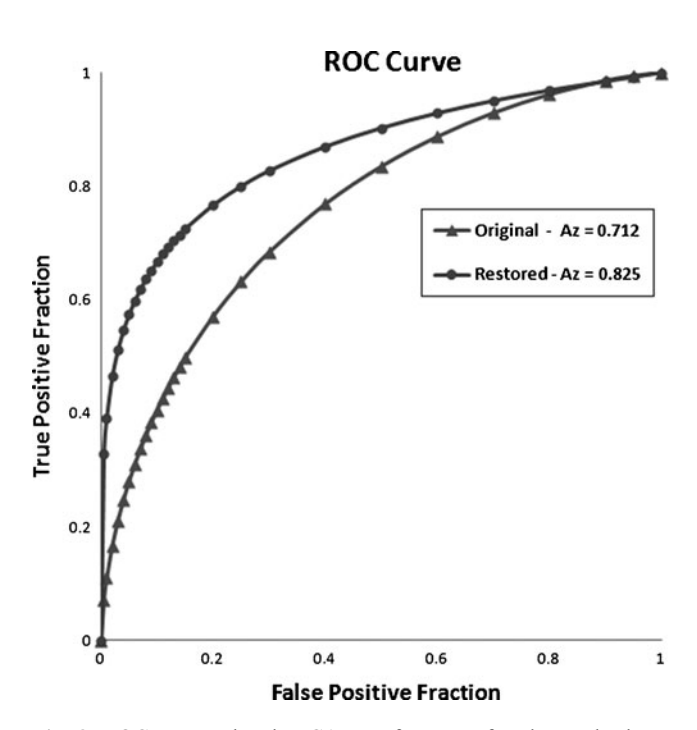


**Fig. 8** ROC curves showing CAD performance for clustered microcalcification detection on the real breast images from hospital no. 1. Degraded images (*filled triangles*) (originally taken with no preprocessing) and restored images (*filled circles*). The parameter Az corresponds to the area under the ROC curve

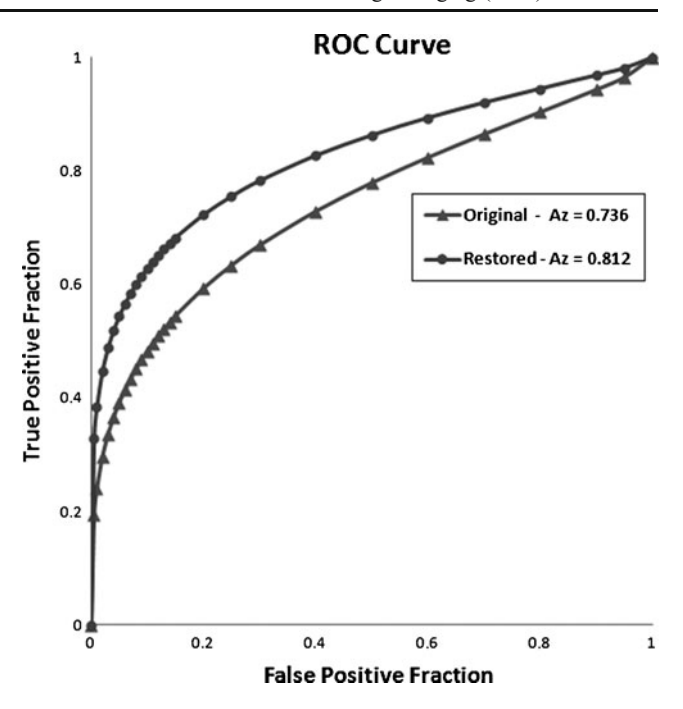


Fig. 9 ROC curves showing CAD performance for clustered micro-calcification detection on the real breast images from hospital no. 2. Degraded images (filled triangles) (originally taken with no preprocessing) and restored images (filled circles). The parameter Az corresponds to the area under the ROC curve

Table 1 shows an increase of up to 11.5 dB (p=0.002) in the PSNR measurements and an increased of up to

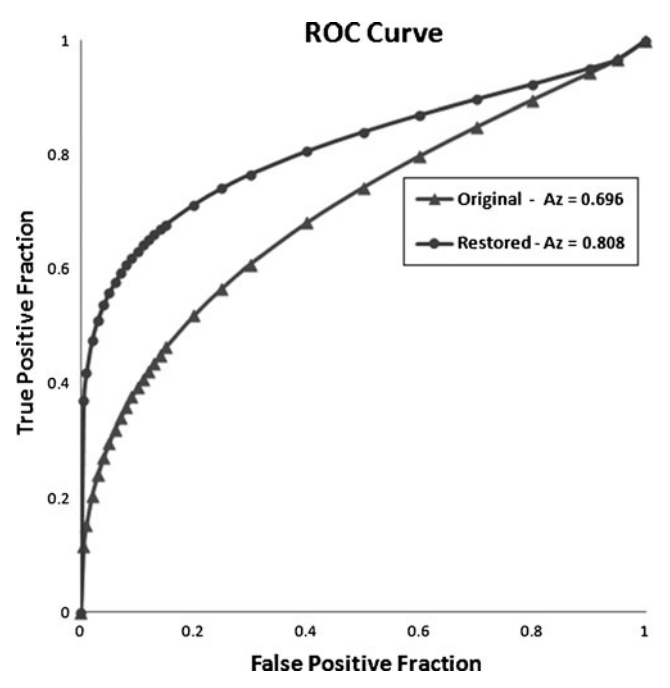


Fig. 10 ROC curves showing CAD performance for clustered micro-calcification detection on the real breast images from hospital no. 3. Degraded images (filled triangles) (originally taken with no preprocessing) and restored images (filled circles). The parameter Az corresponds to the area under the ROC curve



8.3 % (p < 0.001) in the MSSIM index when using our restoration technique. Moreover, we showed that the restored image is visibly less noisy and more similar to the reference image than the degraded one and that image sharpness was preserved after restoration.

We also evaluated the influence of our preprocessing methodology on the performance of a CAD system for the detection of clustered microcalcifications in mammographic images. First, we considered a breast phantom with clustered microcalcifications of known sizes, imaged with different levels of quantum noise. In this case, the ROC analysis suggested that CAD performance was improved when considering our proposed restoration methodology as a preprocessing step. It was observed an average increase of 10.9 % (p=0.04) in CAD performance when using preprocessed images. The restoration methodology yielded an increase in CAD true-positive rates without increasing the false-positive rates, even for images corrupted by a high level of quantum noise. This result shows that the acquisition constraints were, to some extent, overcome by the restoration procedure. This finding could guide a further study of how this restoration could lead to a reduction in the radiation dose on breast cancer screening.

Regarding CAD performance on mammographic images of real breasts, we selected exclusively dense-breast images from a mammography database, which were grouped according to the image acquisition system. Dense-breast images still pose a challenge for CAD systems because such images normally present low contrast between breast tissue and structures associated with breast cancer. In this case, ROC analysis also suggested that our restoration methodology yielded an improvement in CAD performance. Considering all image groups, restoration increased CAD truepositive rates and decreased false-positive rates for clustered microcalcification detection. An average increase of 14.1 % (p=0.01) in CAD performance when using preprocessed images sets was observed. In comparison to other preprocessing techniques for the enhancement of mammographic images, this work presented significant results. Nunes et al. [21] presented an MTF-based filter to enhance dense-breast images and evaluated the improvement of CAD performance for microcalcification detection. An increase of 5.3 % in the area under ROC curve was reported, followed by a little increase in false-positive rates. Papadopoulos et al. [23] compared the improvement of CAD performance for microcalcification detection considering five different image enhancement algorithms: contrast-limited adaptive histogram equalization, local range modification (LRM), and the redundant discrete wavelet linear stretching and shrinkage algorithms. The highest performance gain, considering the area under ROC curve, was about 8.5 % and was observed with the LRM algorithm. In another work, Schiabel et al. [43] reported an increase of about 5 % in CAD

performance using a preprocessing algorithm based on mammography imaging quality parameters.

Because microcalcifications are high-frequency elements within an image, enhancement techniques that emphasize sharp transitions and fine details often yield an increase in image noise. On the other hand, image denoising algorithms typically reduce the contrast of high-frequency elements in the image, which often yields a loss of spatial resolution. However, the results using the combination of an image denoising algorithm followed by an image enhancement procedure in this work reduced image noise without significantly affecting image sharpness.

These results show that Anscombe transformation was efficient at converting the mammography image quantum noise into a Gaussian additive noise, which can be better removed by the Wiener filter. Furthermore, in the Anscombe domain, image noise was removed through an adaptive Wiener filter, whose parameters are obtained considering local image statistics. Consequently, the adaptive filter allowed for noise reduction by a more precise representation of the mean and variance of the pixel under consideration.

The proposed restoration method has one notable characteristic: the use of information about the acquisition system as input data for the restoration procedure. This characteristic implies that each image set will receive a custom preprocessing filter that correlates to the properties of the acquisition system used in the imaging process. Thus, the MTF-based filter yielded a contrast enhancement for high-frequency signals in the image, which led to microcalcifications appearing more visible in the mammographic images, which ultimately improved CAD performance.

Some of the limitations of this paper and future directions are now addressed. One limitation of this study is that all dense-breast images evaluated by our CAD system were taken from screen-film mammography. Although there is an increasing trend toward full-field digital mammography (FFDM), this study still reflects the majority of practices [9, 50]. Another limitation is that we used a previously developed CAD system to evaluate our preprocessing technique, instead of using a commercial CAD system. However, considering that the main objective of this paper is to present and evaluate this novel restoration methodology, the results show that our technique can improve mammography image quality, which can lead to an improvement in the performance of CAD systems. In order to evaluate the clinical application of our methodology in breast cancer screening, further study must be carried out using FFDM images and commercial CAD systems.

## Conclusion

In this paper, we investigated the use of the Anscombe transformation and the adaptive Wiener filter for mammography



image denoising and an MTF-based inverse filter for mammographic image restoration. This image restoration technique could be used as a preprocessing module in computeraided detection systems to improve the detection of microcalcifications in breast cancer screening. The results presented in this paper show that the proposed restoration method produces mammography images with reduced quantum noise, preserving image sharpness.

Regarding CAD performance, the results suggested that the preprocessing improved mammographic images, making them more suitable for the digital processing procedures that are used to detect structures of clinical interest. Using our CAD system, restoration increased the detectability of microcalcifications in mammographic images without increasing the false-positive rates. ROC analysis revealed an increase in overall CAD performance for clustered microcalcification detection when restored image sets were used. A deep investigation using more mammographic images, other types of breast lesions, and other CAD systems must be carried out to evaluate the clinical use of the proposed methodology in breast cancer screening. Moreover, further study of how this restoration could lead to a reduction in the radiation dose used in mammography examinations will be conducted in the future.

**Acknowledgments** The authors would like to thank FAPESP and CAPES for their financial support.

## References

- IARC. World cancer report: International agency for research on cancer. Lyon, 2008
- Elmore JG, Nakano CY, Koepsell TD, Desnick LM, D'Orsi CJ, Ransohoff DF: International variation in screening mammography interpretations in community-based programs. J Natl Cancer Inst 95(18):1384–1393, 2003
- Veronesi U, Boyle P, Goldhirsch A, Orecchia R, Viale G: Breast cancer. Lancet 365:1727–1741, 2005
- Chlebowski RT: Breast cancer risk reduction: strategies for women at increased risk. Annu Rev Med 53:519–540, 2002
- Giger ML, Chan H-P, Boone J: Anniversary paper: history and status of CAD and quantitative image analysis: the role of Medical Physics and AAPM. Med Phys 35(12):5799–5820, 2008
- Boyer B, Balleyguier C, Granat O, Pharaboz C: CAD in questions/ answers review of the literature. Eur J Radiol 69(1):24–33, 2009
- Freer TW, Ulissey MJ: Screening mammography with computeraided detection: prospective study of 12,860 patients in a community breast center. Radiology 220(3):781–786, 2001
- Dean JC, Ilvento CC: Improved cancer detection using computeraided detection with diagnostic and screening mammography: prospective study of 104 cancers. Am J Roentgenol 187(1):20– 28, 2006
- Mahoney MC, Meganathan K: False positive marks on unsuspicious screening mammography with computer-aided detection. J Digit Imaging 24(5):772–777, 2011
- Kopans DB: Breast imaging, 3rd edition. Lippincott Williams & Wilkins, Philadelphia, 2006

- Yoon HJ, Zheng B, Sahiner B, Chakraborty DP: Evaluating computeraided detection algorithms. Med Phys 34(6):2024–2038, 2007
- Acha B, Serrano C, Rangayyan RM, Leo Desautels JE: Detection of microcalcifications in mammograms using error of prediction and statistical measures. J Electronic Imaging 18(1):013011, 2009
- 13. Cole EB, Pisano ED, Kistner EO, Muller KE, Brown ME, Feig SA, Jong RA, Maidment ADA, Staiger MJ, Kuzmiak CM, Freimanis RI, Lesko N, Rosen EL, Walsh R, Williford M, Braeuning MP: Diagnostic accuracy of digital mammography in patients with dense breasts who underwent problem-solving mammography: effects of image processing and lesion type. Radiology 226(1):153–160, 2003
- Birdwell RL, Ikeda DM, O'Shaughnessy KF, Sickles EA: Mammographic characteristics of 115 missed cancers later detected with screening mammography and the potential utility of computer-aided detection. Radiology 219(1):192–202, 2001
- Ho WT, Lam PWT: Clinical performance of computer-assisted detection (CAD) system in detecting carcinoma in breasts of different densities. Clin Radiol 58(2):133–136, 2003
- Chan HP, Niklason LT, Ikeda DM, Lam KL, Adler DD: Digitization requirements in mammography: effects on computer-aided detection of microcalcifications. Med Phys 21(7):1203–1211, 1994
- Nishikawa RM, Giger ML, Doi K, Metz CE, Yin FF, Vyborny CJ, Schmidt RA: Effect of case selection on the performance of computer-aided detection schemes. Med Phys 21(2):265–269, 1994
- Schiabel H, Nunes FL, Escarpinati MC, Benatti RH: Investigations on the effect of different characteristics of images sets on the performance of a processing scheme for microcalcifications detection in digital mammograms. J Digit Imaging 14(Suppl 1):224–225, 2001
- Garcia-Orellana CJ, Gallardo-Caballero R, Gonzalez-Velasco HM, Garcia-Manso A, Macias-Macias M: Study of a mammographic CAD performance dependence on the considered mammogram set. Conf Proc IEEE Eng Med Biol Soc 2008:4776–4779, 2008
- Tourassi GD, Ike R, Singh S, Harrawood B: Evaluating the effect of image preprocessing on an information-theoretic CAD system in mammography. Acad Radiol 15(5):626–634, 2008
- Nunes FLS, Schiabel H, Benatti RH: Contrast enhancement in dense breast images using the modulation transfer function. Med Phys 29(12):2925–2936, 2002
- Mencattini A, Salmeri M, Lojacono R, Frigerio M, Caselli F: Mammographic images enhancement and denoising for breast cancer detection using dyadic wavelet processing. IEEE Trans Instrum Meas 57(7):1422–1430, 2008
- Papadopoulos A, Fotiadis DI, Costaridou L: Improvement of microcalcification cluster detection in mammography utilizing image enhancement techniques. Comput Biol Med 38(10):1045–1055, 2008
- Gonzalez RC, Woods RE: Digital image processing, 3rd edition. Prentice Hall, Upper Saddle River, 2008
- Yaffe MJ: Digital mammography. In: Beutel J, Kundel HL, Van Metter RL Eds. Handbook of medical imaging. Vol 1. Physics and psychophysics. SPIE Press, Bellingham, 2000, pp 329–372
- Saunders RS, Baker JA, Delong DM, Johnson JP, Samei E: Does image quality matter? Impact of resolution and noise on mammographic task performance. Med Phys 34(10):3971–3981, 2007
- Anscombe FJ: The transformation of Poisson, binomial and negative-binomial data. Biometrika 35:246–254, 1948
- Mascarenhas NDA, Santos CAN, Cruvinel PE: Transmission tomography under poisson noise using the anscombe transformation and wiener filtering of the projections. Nucl Instrum Meth A 423:265–271, 1999
- 29. Jin F, Fieguth P, Winger L, Jernigan E: Adaptive Wiener filtering of noisy images and image sequences. In: 2003 International Conference on Image Processing, Proceedings of IEEE Vol 3, New York (USA), 2003, pp 349-352
- Metz CE, Doi K: Transfer function analysis of radiographic imaging systems. Phys Med Biol 24(6):1079–1106, 1979
- Rabbani M: Bayesian filtering of poisson noise using local statistics. IEEE T Acoust Speech 36(6):933–937, 1998



- 32. Doi K: Field characteristics of geometric unsharpness due to the X-ray tube focal spot. Med Phys 4(1):15–20, 1977
- Rossmann K: Point spread-function, line spread-function, and modulation transfer function. Radiology 93(2):257–272, 1969
- 34. NEMA: Measurement of dimensions and properties of focal spots of diagnostic X-ray tubes, NEMA Standards XR 5, 1992
- Nickoloff EL, Donnelly E, Eve L, Atherton JV, Asch T: Mammographic resolution: influence of focal spot intensity distribution and geometry. Med Phys 17(3):436–447, 1990
- Hendee WR, Ritenour ER: Medical imaging physics, 4th edition. Wiley-Liss, New York, 2002
- Rong XJ, Krugh KT, Shepard SJ, Geiser WR: Measurement of focal spot size with slit camera using computed radiography and flat-panel based digital detectors. Med Phys 30(7):1768–1775, 2003
- Tang S, Barnes GT, Tanner RL: Slit camera focal spot measurement errors in mammography. Med Phys 22(11):1803–1814, 1995
- Goes CE, Schiabel H, Nunes FLS: Evaluation of microcalcifications segmentation techniques for dense breast digitized images. J Digit Imaging 15(Suppl 1):231–233, 2002
- Nunes FLS, Schiabel H, Goes CE: Contrast enhancement in dense breast images to aid clustered microcalcifications detection. J Digit Imaging 20(1):53–66, 2007
- Wang Z, Bovik AC: Mean squared error: love it or leave it? A new look at signal fidelity measures. IEEE Signal Proc Mag 26(1):98–117, 2009
- Wang Z, Bovik AC, Sheikh HR, Simoncelli EP: Image quality assessment: from error visibility to structural similarity. IEEE T Image Process 13(4):600–612, 2004

- Schiabel H, Vieira MAC, Ventura L: Preprocessing for improving CAD scheme performance for microcalcification detection based on mammography imaging quality parameters. In: Medical Imaging 2009: Computer-Aided Diagnosis, Proceedings of SPIE Vol 7260, Orlando (USA), pp 72602G1-G12, 2009
- Matheus BR, Schiabel H: Online mammographic images database for development and comparison of CAD schemes. J Digit Imaging 24(3):500–506, 2011
- CIRS Computerized imaging reference systems, Inc. Model 011A manual. Norfolk. VA
- 46. Oliveira Jr PD, Vieira MAC, Schiabel H: Determination of focal spot size and the modulation transfer function of mammographic equipment without previous alignment. In: World Congress on Medical Physics and Biomedical Engineering, Munich (Germany), pp 1186-1189, 2009
- Vieira MAC, Oliveira Jr PD, Schiabel H: Computational method for automatic determination of radiographic equipment anode angle. In: Medical Imaging 2008: Physics of Medical Imaging, Proceedings of SPIE Vol 6913, San Diego (USA), pp 69133 M1-M8, 2008
- 48. Metz C: ROC analysis in medical imaging: a tutorial review of the literature. Radiol Phys Technol 1:2–12, 2008
- Eng J. ROC analysis: web-based calculator for ROC curves. Baltimore: Johns Hopkins University [updated 2006 May 17]. Available from: http://www.jrocfit.org
- Glynn CG, Farria DM, Monsees BS, Salcman JT, Wiele KN, Hildebolt CF: Effect of transition to digital mammography on clinical outcomes. Radiology 260(3):664–670, 2011

